Shape Memory Alloy / Glass Composite Seal for Solid Oxide Fuel Cells

Christopher B. Story

Thesis submitted to the faculty of the Virginia Polytechnic Institute and State University
in partial fulfillment of the requirements for the degree of

Master of Science
In
Materials Science and Engineering

Committee:

Dr. Kathy Lu, Chair
Dr. W. T. Reynolds, Jr.
Dr. Gary Pickrell

May 8, 2007
Blacksburg, VA

Keywords: Solid Oxide Fuel Cell, Gas Sealant, Shape Memory Alloy, TiNiHf, SrO-La_2O_3-Al_2O_3-B_2O_3-SiO_2, 3D Printing, Rapid Prototyping

Shape Memory Alloy / Glass Composite Seal for Solid Oxide Fuel Cells

Christopher B. Story

ABSTRACT

Widespread use of solid oxide fuel cells is hindered by a lack of long-term durability of seals between metallic and ceramic components caused by thermal expansion mismatch induced cracking. A novel gas seal design incorporating an engineered thermal expansion gradient in a SrO-La_2O_3-Al_2O_3-B_2O_3-SiO_2 glass matrix with a TiNiHf shape memory alloy mesh for active stress relief and crack healing is being developed. Coefficient of thermal expansion (CTE) measurements of the seal and fuel cell components shows the possibility for a thermal expansion gradient. Differential scanning calorimetry and microscopy have shown that the TiNiHf alloy has a shape memory transition in the desired range of 200-250ºC. The oxide glass partially crystallizes during thermal cycling which has been observed through X-ray diffraction and dilatometry. The CTE decreases from 9.3×10^{-6}/°C to 6.6×10^{-6}/°C after thermal cycling. Neutron diffraction data from TiNiHf /glass composite samples reveals that the TiNiHf alloy has the ability of absorbing residual stresses from a glass matrix during martensitic phase transition. There is evidence from microscopy that the glass composition is important in determining if reaction will occur with the TiNiHf alloy. The TiNiHf alloy mesh structures can be created using the 3D printing process. This process has been adapted to allow for printing of very thin wire mesh structures of Ni and NiTi powders with a more suitable binder solution. A bi-layer test fixture has been developed which will be useful for assessing leak rate through seal materials.

Table of Contents

MULTIMEDIA OBJECTS V

GRANT INFORMATION VI

AUTHOR'S ACKNOWLEDGEMENTS VII

LIST OF SYMBOLS VIII

INTRODUCTION 1

MATERIALS PREPARATION 3

TiNiHf Alloy 3

$SrO\text{-}La_2O_3\text{-}Al_2O_3\text{-}B_2O_3\text{-}SiO_2$ Glass-Ceramic 4

MATERIALS CHARACTERIZATION 4

Differential Scanning Calorimetry of TiNiHf Alloy 4

XRD of SLABS Glass/Ceramic 6

Dilatometry Testing 7

NEUTRON DIFFRACTION 10

Sample Preparation 10

Diffraction Results 10

3D PRINTING 16

Overview of Process 16

Metal Powders 17

Binder Development 19

NiTi Powders 22

BI-LAYER TEST FIXTURE DEVELOPMENT 23

SMA / SLABS SINTERED POWDERS 25

Sample Preparation 25

Optical Microscopy of SMA/SLABS Sintered Samples 25

Electron Microscopy and EDS 27

CONCLUSIONS 31

REFERENCES 33

VITA 34

Multimedia Objects

Figure 1 Schematic of Planar SOFC Design Showing Multiple Layers. 1

Figure 2 Differential Scanning Calorimetry of the NiTiHf Ingot Showing Martensite-Austenite Phase Transition. 5

Figure 3 Optical Micrograph of the NiTiHf Ingot Showing Martensitic Lath Microstructure. 6

Figure 4 X-ray Diffraction of SLABS Glass/Ceramic in As-Cast Condition and Thermally Cycled 4 Times between RT and 800 °C. 7

Figure 5 Dilatometry curves from: (a) E-brite stainless steel, an interconnect material, (b) Sc-ZrO_2, an electrolyte material, (c) the NiTiHf alloy, and (d) the SLABS Glass/Ceramic; (c) and (d) are the components of the composite seal. 9

Figure 6 Neutron Diffraction Patterns of NiTiHf/Glass Composite Sample Cooled at 5 °C/min at 3 Temperatures. Martensite (020)/(012) Double Peak and Austenite (110), (111), and (210) Peaks Indicated. 12

Figure 7 Normalized Intensity of (110) Austenite Peak Cooled at Different Rates. 13

Figure 8 D-Spacing of (110) Austenite Peak Cooled at Different Rates. 15

Figure 9 Average Shift in Austenite Unit Cell Volume between bare SMA and SMA/glass samples. Calculated from d-spacing of (110), (210), and (111) Planes. 15

Figure 10 Rheology of S-binder and AE2 Binder 22

Figure 11 Pure Ni (left) and NiTi (right) powders 23

Figure 12 Design of Bi-layer Test Fixture 24

Figure 13 E-brite stainless steel Cu-Zn brazed to ¼" stainless steel tubing 25

Figure 14 Optical Micrograph of 10wt% NiTiHf Sintered Sample 26

Figure 15 Optical Micrograph of 40wt% NiTiHf Sintered Sample 27

Figure 16 Optical Micrograph of reaction zone around NiTiHf particles in 10wt% NiTiHf sample 27

Figure 17 SEM micrograph and EDS line scan of 10wt% SMA sintered composite 30

Table 1 Major Variables used in 3D Printing 16

Table 2 Binder Solutions Examined 21

Grant Information

This material is based upon work supported by the Department of Energy National Energy Technology Laboratory and National Nuclear Security Administration under Award Numbers DE-FG26-06NT42741 and DE-FC07-06ID14739, respectively.

Author's Acknowledgements

I would like to thank Don Brown, Scott Williams, Tomas Sisneros, and Saurabh Kabra at Los Alamos National Laboratory, NM, for their help performing the neutron diffraction tests. I also thank Kai Zhang for performing X-ray diffraction experiments, Manoj Mahapatra for analyzing X-ray diffraction results, Steve McCartney for helping conduct scanning electron microscopy, and Dave Berry for his expertise and advice, all from Virginia Tech. Finally, my advisors Dr. Kathy Lu and Dr. W. T. Reynolds have been of great help at keeping me motivated and in solving the continual problems involved in research.

List of Symbols

a: Cubic Lattice Constant

α: Coefficient of Thermal Expansion (CTE)

T_g: Glass Transition Temperature

A_s: Austenite Start Temperature

A_f: Austenite Finish Temperature

M_s: Martensite Start Temperature

M_f: Martensite Finish Temperature

Introduction

Planar Solid Oxide Fuel Cells (SOFC) hold great promise for clean power generation in stationary applications but have been hindered from widespread commercialization by a lack of long term durability. A major cause of limited durability is cracking of the seals between cell components during thermal cycling and subsequent leakage of the fuel and oxidizing gases. SOFCs of the planar design contain both metallic and ceramic components which must have a hermitic seal at the perimeter between layers. Figure 1 is a schematic design of a planar SOFC showing the multiple layers. The interconnect material is typically a stainless steel alloy while the other components are ceramic or cermets. For an electrolyte supported SOFC design, the gas sealant would connect the stainless steel interconnect with a doped zirconia electrolyte.

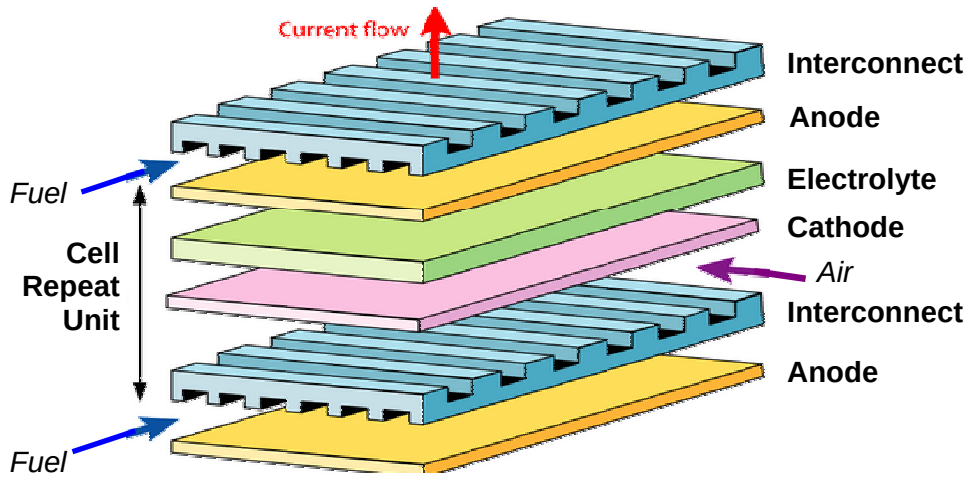

Figure 1 Schematic of Planar SOFC Design Showing Multiple Layers[1].

Many seal materials have been investigated including Ag brazing, glasses, glass-ceramics, and mica[2,3,4,5,6]. A suitable seal material must be: chemically stable at fuel cell operating temperatures in both high and low oxygen partial pressures, non-reactive with

other cell components, mechanically stable, electrically insulating, and finally able to accommodate thermal expansion mismatch between cell components. It is very important to create a gas seal that satisfies these requirements so that SOFCs can be further developed.

The SOFC operating temperature range is 800-1000ºC and rapid heating and cooling rates are desired. For glass seals, the operating temperature must be above the seal's glass transition temperature, T_g, for the seal to be mechanically compliant, but the glass must also have a relatively high viscosity to withstand the gas pressure in the cell. Upon cooling after operation, gas seals are prone to cracking from thermal stresses caused by a mismatch in the coefficients of thermal expansion (CTE) between the cell components. To prevent cracking in the glass seals the "general axiom is that $\Delta\alpha = \alpha_{metal} - \alpha_{glass}$ should not exceed $1\times10^{-6}\,K^{-1}$."[7] At the stack-to-manifold junction in a SOFC the glass seal must accommodate a 20% mismatch in CTE[8].

The goal of this project is to explore the feasibility of a composite seal that integrates a metallic shape memory alloy (SMA) into a glass/ceramic matrix. This composite seal incorporates two design ideas. First, a gradient in the ratio of metal to glass is introduced across the seal thickness to create a gradient thermal expansion coefficient and lower thermal stresses. Second, a high temperature shape memory alloy is chosen for the metal in the composite to take advantage of its transformation strains to offset thermal stresses in the seal. The SMA was chosen for its ability to exert large stresses when returning to its undeformed shape during the martensite-austenite phase change at 200-250ºC. In addition, the shape memory effect during heating to the operating temperature has the potential of closing cracks that may have formed in the seal

during a previous cooling cycle. The glass/ceramic selected for the seal is the SrO-La_2O_3-Al_2O_3-B_2O_3-SiO_2 system chosen from a previous study conducted by Ley et al because of its relatively high CTE and high glass transition temperature (T_g)[8]. A $Ti_{36}Ni_{49}Hf_{15}$ alloy was selected for the shape memory component of the seal because of the relatively high temperature range for the austenite/martensite transitions[9].

Materials Preparation

TiNiHf Alloy

$Ti_{36}Ni_{49}Hf_{15}$ SMA ingots were produced by arc-melting Ti sponge (99.95% purity, Alfa Aesar, Ward Hill, MA), Ni lump (99.99% purity, Atlantic Equipment Engineers, Bergenfield, NJ), and Hf rod (99.95% purity, Fine Metals Corporation, Ashland, VA) in a water-cooled copper crucible under an argon atmosphere. Two ingots, 38 x 76 x 13 mm in size, were made with this procedure. The ingots were homogenized in vacuum for 24 hours at 1075°C and then at 1150°C for 48 hours before being water quenched.

Atomization of $Ti_{35}Ni_{50}Hf_{15}$ SMA powder was carried out at Crucible Research (Pittsburgh, PA) using a 5kg charge and in a laboratory gas atomizer. The starting materials were virgin metals including 99.99% Ni and Ti, plus Hf (Fine Metals). The molten metal was injected through a 6.35mm diameter nozzle and atomized with a high-pressure argon gas stream, delivered from an annular gas delivery die surrounding the nozzle bore. Cooling rates for this atomizer are typically at 1,000-10,000°C/s depending on particle size and other variables. The majority of the TiNiHf powder was collected in a pool of liquid argon (to prevent sintering), while finer particles were removed from the exhaust by a cyclone scrubber.

SrO-La_2O_3-Al_2O_3-B_2O_3-SiO_2 Glass-Ceramic

A glass composition of $25SrO\text{-}20La_2O_3\text{-}7Al_2O_3\text{-}40B_2O_3\text{-}8SiO_2$ mol%, was produced by mixing and milling the oxide powders and melting in a platinum crucible at 1400°C for 3 hours. The molten glass was then poured into water to produce frit or into a graphite mold for producing dilatometry samples of 1" length and ~0.25" diameter.

Materials Characterization

Differential Scanning Calorimetry of TiNiHf Alloy

The SMA ingot was analyzed with a Netsch 449C DSC/TGA analyzer to determine the temperature range of the austenite to martensite phase transformation. Samples cut from the bulk ingot approximately 10-15 mg in size were heated in helium between 50ºC and 375ºC at 10ºC/min.

The arc-melted ingot showed no shape memory effect after ingot solidification. After homogenization, the ingot showed distinct peaks during heating and cooling for the martensite-austenite phase change (Figure 2). The temperatures of the martensite to austenite transformation on heating and the austenite to martensite transition on cooling shifted slightly as the alloy underwent several thermal cycles. The low-temperature side of the DSC peak on heating was taken to be the austenite start temperature, or A_s , and the high-temperature side was interpreted as the austenite finish temperature, or A_f . The A_s of the first and fourth heating cycles were approximately 250ºC and 225ºC, respectively. The A_f of the first and fourth heating cycles were 290ºC and 250ºC, respectively. Similarly, the martensite start and finish temperatures, M_s and M_f , were obtained from the high-temperature and low temperature sides of the peaks on the DSC

cooling curves (Figure 2). Thermal cycling lowered the M_s temperature from approximately 210 to 200ºC and the M_f temperature from 180 to 170ºC. Figure 3 is an optical micrograph of a polished SMA sample showing surface relief from martensite laths.

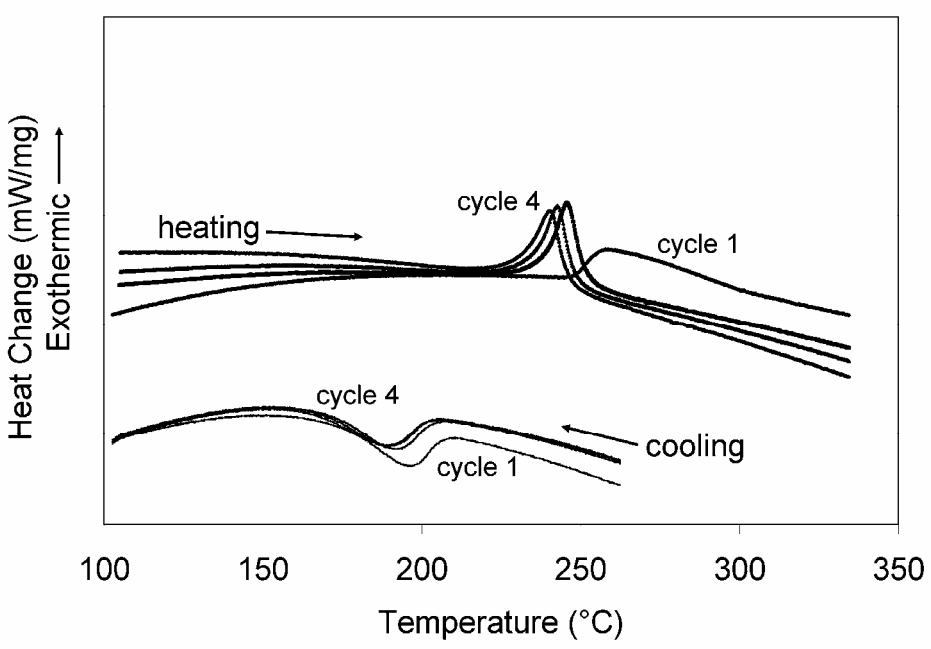

Figure 2 Differential Scanning Calorimetry of the NiTiHf Ingot Showing Martensite-Austenite Phase Transition.

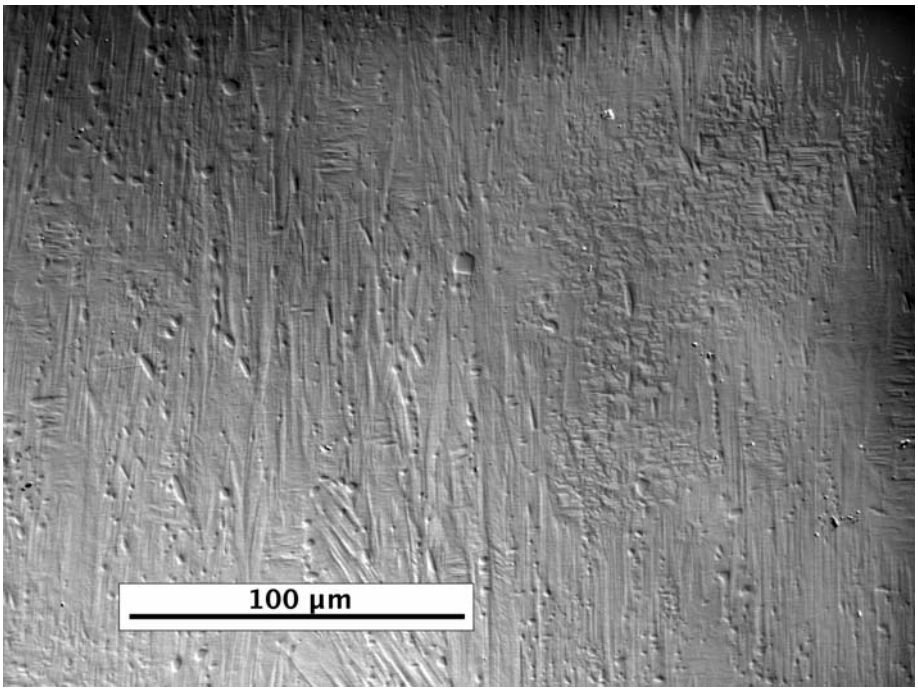

Figure 3 Optical Micrograph of the NiTiHf Ingot Showing Martensitic Lath Microstructure.

XRD of SLABS Glass/Ceramic

Crystalline phase identification of the as-cast and thermally cycled SLABS glass was conducted by X-ray powder diffraction (XRD) on a Rigaku X-ray diffractometer using Cu Kα radiation. Both samples were quenched in a graphite mold, and the thermally cycled glass followed the same profile as the dilatometry sample.

Figure 4 is the XRD patterns of the as-cast and thermally cycled SLABS glass. XRD analysis showed that the SLABS glass was mostly amorphous in the as-cast condition with a small amount of $La_2Sr_3(BO_3)_4$ present. After four thermal cycles, $La_2Sr_3(BO_3)_4$ crystalline phase substantially increased, along with the appearance of $SrLaBO_4$ phase and some un-identified peaks. B_2O_3 is the major glass former in this composition and the 7 at% alumina addition in this glass serves to reduce crystallization. From XRD analysis, it is apparent that 7 at% is not sufficient to avoid devitrification, and work is being conducted now to determine how higher Al_2O_3 content affects devitrification.

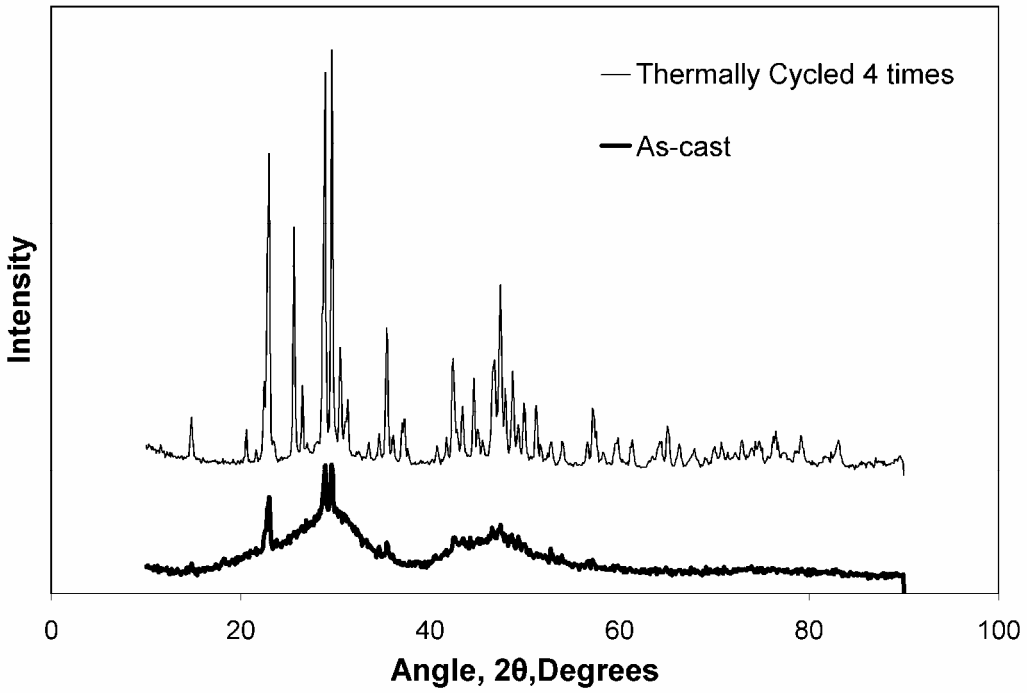

Figure 4 X-ray Diffraction of SLABS Glass/Ceramic in As-Cast Condition and Thermally Cycled 4 Times between RT and 800 ºC.

Dilatometry Testing

A push rod dilatometer (Orton 1600B, Edward Orton Jr. Ceramic Foundation, Westerville, Ohio) was used to measure thermal expansion coefficients. The CTE of the TiNiHf shape memory alloy and the SLABS glass was measured at 5°C/min heating and cooling rates from 50ºC to 800ºC. Sc-stabilized ZrO_2 electrolyte, from Ceramatec (Salt Lake City, Utah) and ferritic stainless steel interconnect material (E-Brite) from ATI Allegheny Ludlum (Pittsburgh, PA) were tested at 3°C/min heating and cooling rates between 50 and 800°C.

Thermal expansion data for the component materials in a solid oxide fuel cell stack are presented in Figure 5. The dilatometry curves and the average thermal expansion coefficient calculated from the slope of these curves are shown for a stainless steel interconnect material (Figure 5a), a zirconia electrolyte (Figure 5b), and the

$Ti_{36}Ni_{49}Hf_{15}$ SMA (Figure 5c). The X-ray diffraction results described previously show the SLABS glass crystallizes during thermal cycling; this is consistent with the changing CTE observed as the SLABS glass undergoes thermal cycling, Figure 5d. The SLABS CTE during the first heating excursion from 200-500ºC was 9.3×10^{-6}/°C, and for the 2nd to 4th thermal cycles the CTE between 200-500ºC dropped to 6.6×10^{-6}/°C. The 50% reduction in CTE resulted from crystallization (devitrification) at the highest temperatures of the first thermal cycle; crystallization was also responsible for the negative slope during the first heating from 650-750°C. To be a suitable seal material, the glass must have a CTE similar to the electrolyte, and the reduction in CTE from crystallization makes the CTE mismatch unacceptably large. Future work on the SLABS glass, as stated in the previous section, will focus on suppressing crystallinity to ensure a constant CTE after cycling.

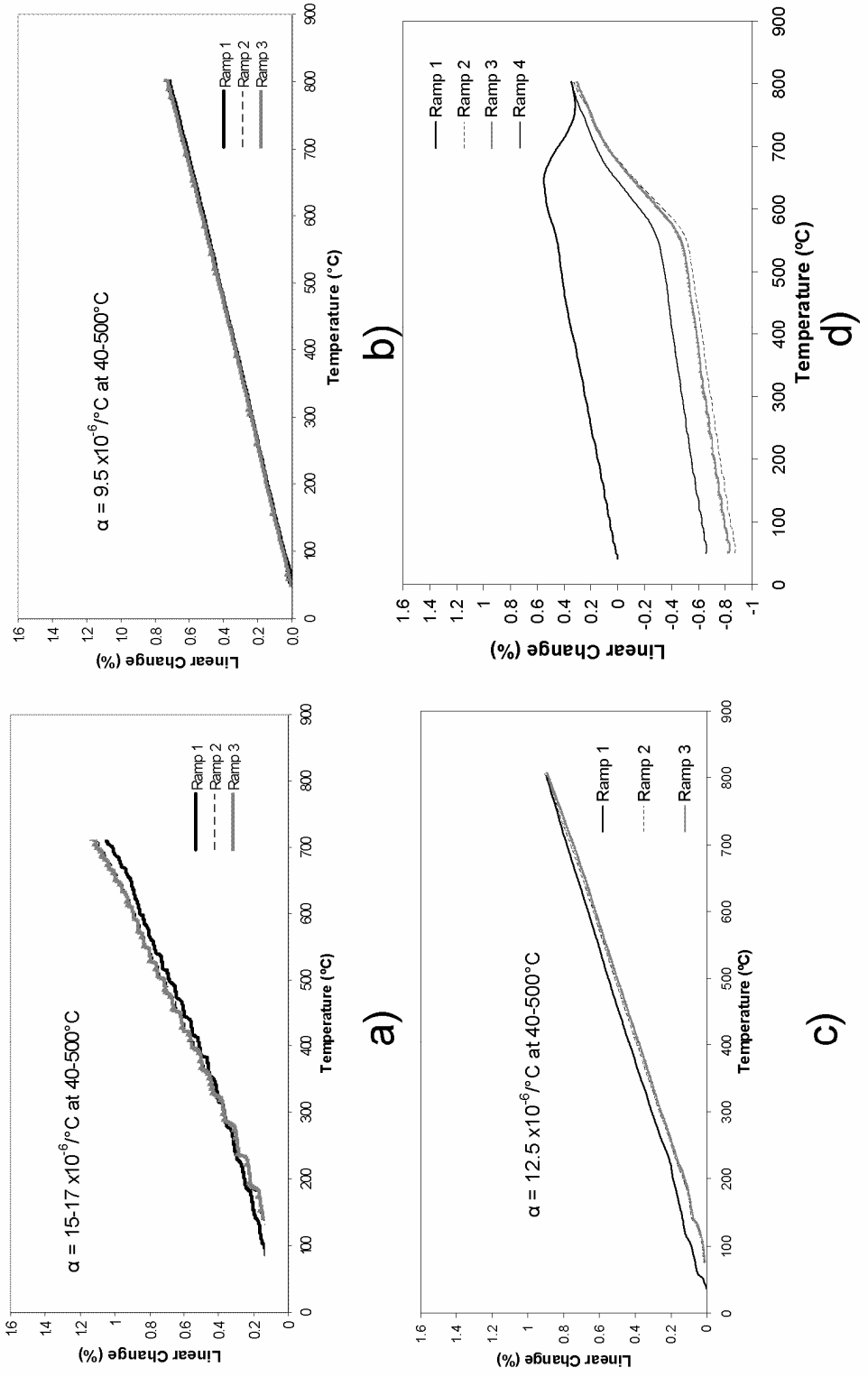

Figure 5 Dilatometry curves from: (a) E-brite stainless steel, an interconnect material, (b) Sc-ZrO_2, an electrolyte material, (c) the NiTiHf alloy, and (d) the SLABS Glass/Ceramic; (c) and (d) are the components of the composite seal.

Neutron Diffraction

The SMARTS system in the Lujan Center at Los Alamos National Laboratory, NM was used for neutron diffraction of SMA/SLABS composite samples. Samples were placed free standing on a graphite base in the chamber of a vacuum furnace. They were heated at 15ºC/min to 800ºC and then cooled at different rates. Analysis of the diffraction data was performed using the SMARTSware software package (LANL, NM).

Sample Preparation

To create neutron diffraction samples of a glass-SMA composite, slivers of the homogenized TiNiHf alloy ingot approximately 1 mm × 1 mm × 20 mm were cut and embedded in a boron-free glass (to avoid excessive neutron absorption). The glass composition was 35wt% SrO-65wt% SiO_2 and the oxide components were mixed and milled before melting. The batches were melted at 1675ºC in a Pt crucible and poured into a 15 mm diameter by 10 mm length graphite mold. The graphite mold contained five SMA slivers supported by holes in the base of the mold. Since cracks were observed in the as-cast composite SMA/glass samples, they were annealed by heating and cooling at 10ºC/min to 850ºC with no hold. This annealing operation healed the cracks and changed the color of the glass from clear to slightly opaque. For a reference sample, a glass cylinder with no SMA slivers was cast and annealed identically.

Diffraction Results

Figure 6 shows three neutron diffraction patterns of the SMA/glass composite sample during cooling at different temperatures with arrows pointing to the different peaks that were analyzed. The austenite phase for $Ti_{36}Ni_{49}Hf_{15}$ is cubic B2 with Ni and Ti occupying different sites and Hf substituting for Ti in the structure. The martensite

phase is monoclinic B19′. Since the composition is near 50Ni-50Ti, the intermediate R phase is not expected[10]. The large background noise was from glass scattering, and diffraction of annealed pure glass was conducted to ensure there were no peaks from crystalline phases to confound interpretation of the data. As shown in Figure 6, martensite peaks were barely visible at 180°C. As the temperature was decreased to 162°C and 124°C, the martensitic (101) and (020)/(012) double peak intensity increased as the proportion of martensite in alloy increased.

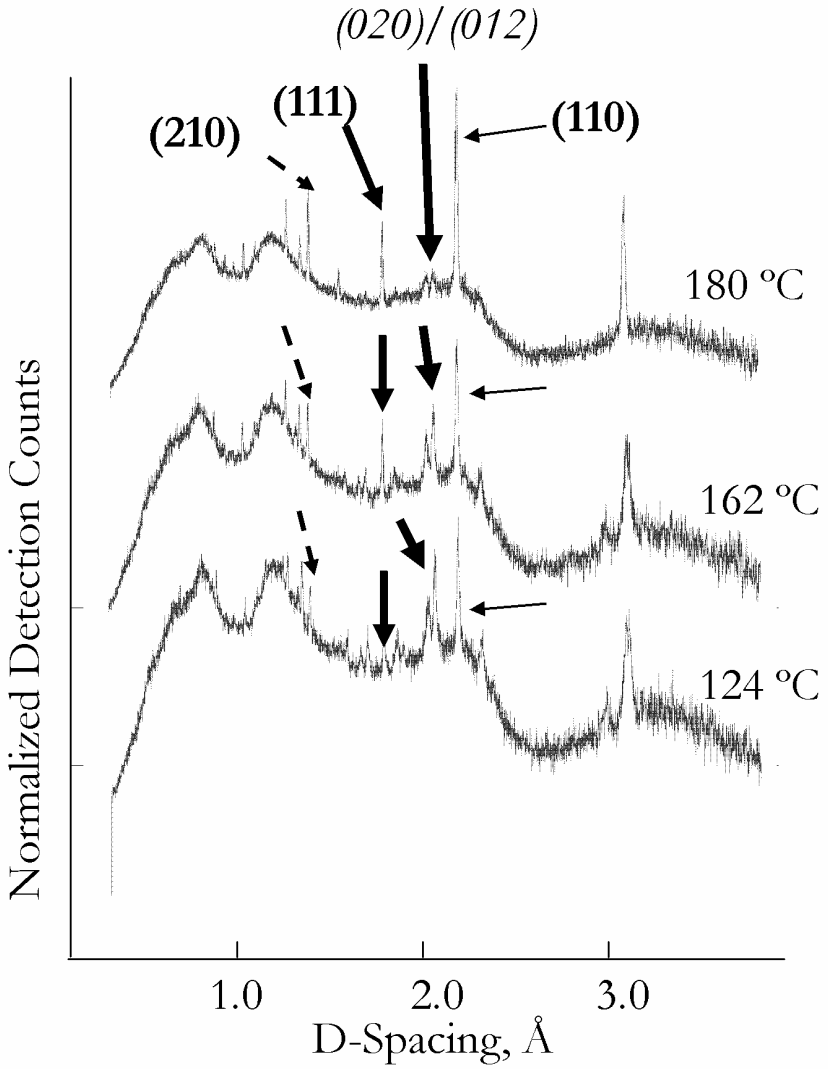

Figure 6 Neutron Diffraction Patterns of NiTiHf/Glass Composite Sample Cooled at 5 ºC/min at 3 Temperatures. Martensite (020)/(012) Double Peak and Austenite (110), (111), and (210) Peaks Indicated.

Peak Intensity

Normalized (110) austenite peak intensity is plotted in Figure 7 for the three diffraction tests: the SMA/glass composite cooled at 5°C/min, the SMA/glass composite cooled at 30°C/min, and bare SMA cooled at 15°C/min. The peak intensity for each test was normalized by considering the detection count at the highest temperature as having a value of unity, and all subsequent detections as a ratio against this detection count. After

the austenite to martensite phase transformation, the austenite peaks are still apparent, indicating that there is still retained austenite in the sample. The error bars on the points reflect the maximum and minimum temperatures at the thermocouple below the sample during the ~30 minute detection period.

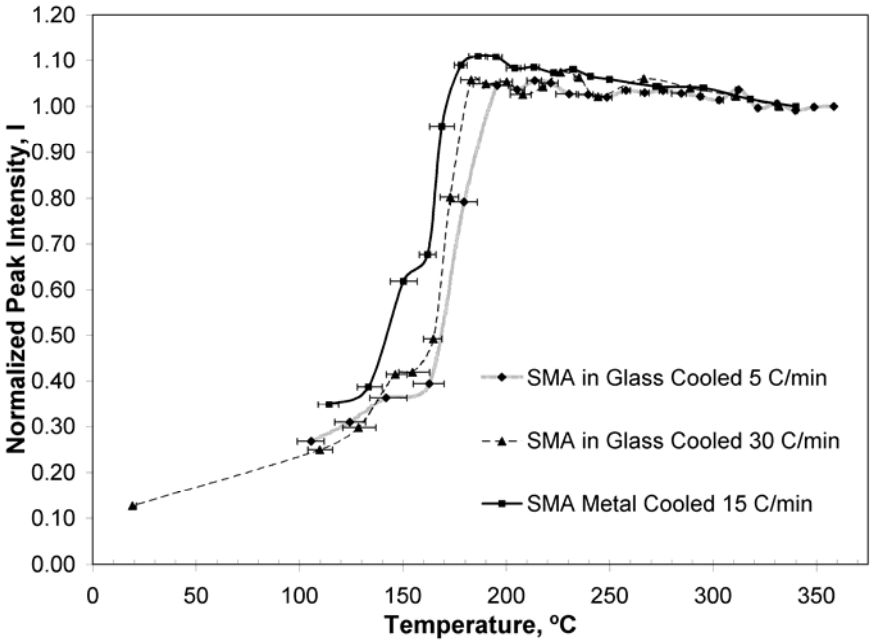

Figure 7 Normalized Intensity of (110) Austenite Peak Cooled at Different Rates.

Peak D-Spacing

The interplanar spacing of the (110) austenite peak as a function of temperature is plotted in Figure 8 for the three tests; plots of the d-spacings of the (210) and (111) austenite peaks show similar trends. It is evident in Figure 8 that for temperatures above the M_s temperature (200ºC), there is a constant offset between the d-spacing of the SMA (110) planes in the composite relative to the same planes in the bare SMA. Because the absolute value of a particular d-spacing is somewhat sensitive to the position of the sample in the diffractometer[11], the difference between d_{110} in the composite and in the

bare metal cannot be interpreted reliably. If the shift is due solely to sample misplacement then the shift would be independent of temperature. This is not the case below the martensite transformation, as the difference between the d-spacings found in the composite versus the bare metal decreases slightly. To quantify this change in d-spacing offset, the unit cell volume was calculated independently for the (110), (210), and (111) planes, assuming the cell remains cubic. The unit cell percent volume difference between the bare SMA and the SMA in glass could be calculated from each plane at each detection temperature. Because the detection temperatures for the bare SMA and SMA/glass samples were not identical, a regression for the bare SMA above and below the M_s temperature was calculated for use in this offset calculation. The regression was not extrapolated beyond the minimum detection temperature for the bare SMA. The percent volume difference was averaged from the values calculated from each plane and is shown in Figure 9. It is seen that the offset *changes* upon cooling from austenite to martensite (the samples were not moved during cooling) implying the residual stresses found in the composite change with temperature. The change may be attributed to a partial relief of residual stress in austenite when it transforms to martensite upon cooling. At temperatures above 200ºC, residual stresses in the composite exert a force on the SMA slivers in the composite. As the composite is cooled, the martensitic phase change and twin motion within martensite provides a deformation mechanism that reduces these residual stresses. This suggests the shape memory effect may be utilized to absorb some of the elastic energy in the glass matrix generated by the CTE mismatch and provide a degree of transformation toughening. The full strain tensor for the SMA in glass cannot be computed from the current data so the magnitude of this possible residual stress cannot

be determined. Experiments could be conducted where a SMA sliver is loaded uniaxialy and both detection banks could be used to determine differences in the stress state resulting from glass thermal stresses.

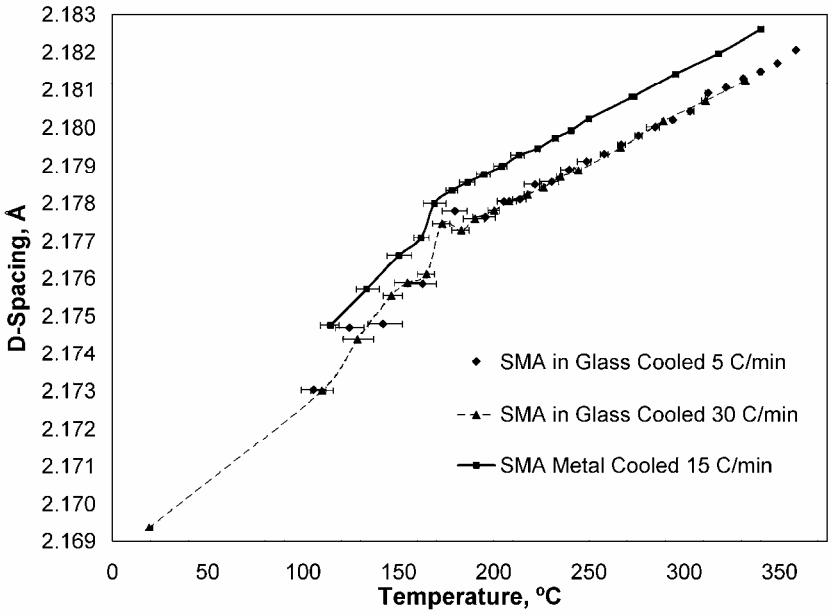

Figure 8 D-Spacing of (110) Austenite Peak Cooled at Different Rates.

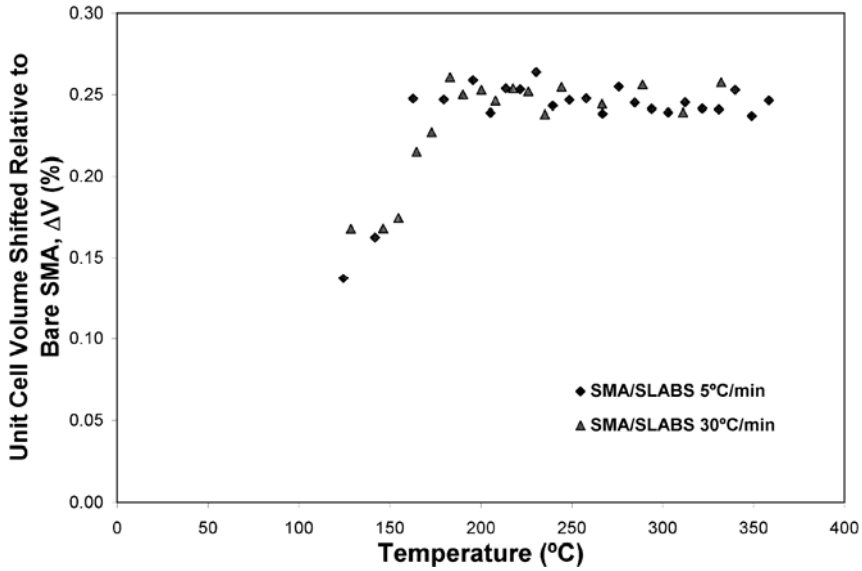

Figure 9 Average Shift in Austenite Unit Cell Volume between bare SMA and SMA/glass samples. Calculated from d-spacing of (110), (210), and (111) Planes.

CTE Estimate

The D-spacing of the austenite (110) peak showed a linear change with temperature down to the martensitic phase transformation starting temperature (Figure 8). The slope of the curve above the martensitic phase transformation starting temperature is 2.6×10^{-5} Å/ºC. An estimate of coefficient of thermal expansion can be calculated from the relationship, $\alpha = \frac{1}{a}\cdot\frac{da}{dT}$. For the SMA at above the martensitic phase transformation starting temperature, $\alpha \approx 12.1\times10^{-6}$/°C, which is in very good agreement with the CTE measured macroscopically with dilatometry.

3D Printing

3D printing is a rapid prototyping technique which can be utilized to create complex shapes quickly. In this study, 3D printing was used to make wire meshes which will be integrated with the SLABS glass to make composite samples.

Overview of Process

The Prometal RX-1 prints a binder strengthened part from metal powders with a maximum size of approximately 2.75"x2"x1" and the strength and resolution of the part are mostly determined by the variables chosen for printing. The table below lists the major variables for 3D printing, their range, and how they can affect the part.

Table 1 Major Variables used in 3D Printing

Name	Range	Details	Effect
Spreader Part Traverse Speed	1.0-5.0 mm/sec	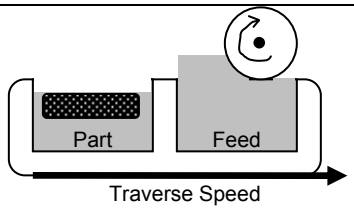	Affects smoothness of powder layer on surface of part box.

Feed Powder to Layer Thickness Ratio	1.0-2.0	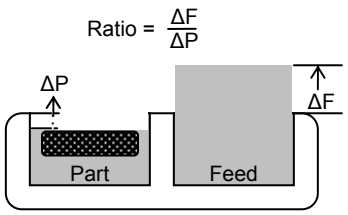	High enough ratio needed to ensure entire part build box covered with layer. Ratio determined by particle size and layer thickness.
Drying	0-90 sec 0-100% heater power	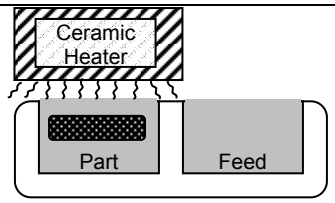	Binder determines time and heater power needed to harden layers before next layer spreading.
Desired Saturation	40-200%	Volumetric percent of liquid printed per layer as compared with volume of void space between particles. Powder packing percent needed for this calculation.	High saturation needed to create strong bonds between particles, but saturation too high creates lateral spreading losing resolution.

Metal Powders

Stainless Steel Parts

Original printing of stainless steel parts used a 420 stainless steel of particle size 45-60 μm and the Prometal S-type binder to print 100 μm thick layers. For printing 100 μm layers, printing variables can be maximized to print layers quickly. The spreader part traverse speed can be set to 3.0-4.0 mm/sec depending on desired resolution, and since thick layers do not require a high feed powder to layer thickness ratio, 1.25 is satisfactory. The desired saturation can be 45% and fully wet the particle surfaces, and finally using the S-type binder for thick layers does require the drying power control setting to be set at 90-100% for between 45-60 seconds. After printing, S-binder parts require a pre-cure of >60 minutes at full heater power before part removal, and a subsequent cure of 2 hours at 180 °C to create the highest green strength.

Ni Printing

Two different nickel powders were used, PM110 (1-2 μm) and high density nickel powder, HDNP (8-15 μm), both from Inco Special Products (Wyckoff, NJ). Nickel powders were chosen with a finer particle size than stainless steel powders, because a goal in printing is feature refinement which is only possible with thinner layer printing. If a 50 μm layer is desired from 420 SS (45-60 μm) then each layer would only be one particle in thickness and this will not create a structurally rigid part. A 10 μm powder would have ~5 particle thick layers making a more even and strong part.

It was found that PM110 can not be spread into thin even layers. The powder has such a low packing that the spreader roller presses the powder into the previous layers in the print bead because the powder will not flow smoothly. Printing was tried at 25 μm, 50 μm, and 100 μm but smooth layers could not be achieved. The powder was heated above 100ºC and then printed to test if the lack of flow was due to adsorbed water but the spreading was still inconsistent. Ball milling with zirconia was tried to break up agglomerates but with no effect.

HDNP spread much better into thin layers. The spreader traverse speed needed to be slowed down to 2.0 mm/sec and the powder to layer thickness ratio needed to be increased to 1.75 for 50 μm layers and 2.00 for 25 μm layers. S-type binder was first used keeping the printing variables similar to SS printing but the parts crumbled during powder removal with a soft paint brush or gentle compressed air. 25 μm and 50 μm layer parts were printed with Prometal's N-type binder but the parts still had very low strength.

In an effort to increase part strength, the desired saturation was increased several times from 55% to 115%. The HDNP has much lower powder packing, requiring more binder to fully wet the particles. Increasing the saturation did cause an increase in

strength, but not enough so that parts could be removed from the powder bed without wires breaking. After consulting Prometal, it was realized that the desired saturation would need to be increased well above 100%, possibly as high as 180% to make the part structurally stable. A problem with this approach is that increasing the saturation causes an increase in lateral spreading. High saturation causes the binder to spread out laterally, causing a 500 μm diameter wire to spread to be much thicker, thus losing the resolution for fine parts. This might be acceptable for printing thicker wires, but to refine wire dimensions, a new binder solution needed to be developed.

Binder Development

Prometal (Irwin, PA) provided two binder solutions, S-type and N-type, for printing stainless steel and nickel powders, respectively. Both binders, when used with fine (10-15 μm) Ni or NiTi powder, created parts of insufficient strength so a study was done to create a new binder solution better suited for fine powders. Poly-acrylic acid (PAA), Darvan-C (PMA), polyvinyl alcohol (PVA), polyethylene glycol (PEG), and an acrylic emulsion (AE) were studied.

Polyacrylic Acid and Polymethacrylic Acid

The first binder examined was a 2.4 vol% PAA (2000 M.W.) aqueous solution with a 20 wt% glycerol addition (based on PAA solids) which was based on a previous 3D printing study[12]. This binder created parts weaker than N-type or S-type binder under similar saturation.

Several solutions were then made with 10-40 vol% PMA and 10-40% glycerol, and droplets were placed on a Ni powder bed and cured at 170 °C for 2 hr but all of the solutions were weaker than S-binder droplets. A 1 mm wire thickness mesh was printed

with a 40 vol% PMA, 10 vol% glycerol solution, but the part crumbled under a paint brush after curing.

It was then tried to increase the PAA content in S-type or N-type binders, so 1-3 vol% PAA was added to S-type and N-type binders. A white solid formed in both solutions immediately on PAA addition and the solid could not be put back in solution by addition of glycerol, stirring, or heating. Solutions were also made by adding small additions of PMA (1-3 vol %) to S-type binder with and without glycerol but a similar white solid formed which was insoluble. Even if PAA or PMA were dissolved in ethanol before mixing with S-type binder, a white solid would still form.

Polyvinyl Alcohol, Polyethylene Glycol, and Acrylic Emulsion

PVA and PEG were acquired from Alfa Aesar (Ward Hill, MA) and an acrylic emulsion, GAC-200, was acquired from Golden Artist Colors (New Berlin, NY). Solutions were made as shown in Table 2. The PVA had a high MW, and was difficult to fully dissolve due to inexperience with PVA solutions. For the PEG and AE solutions, droplets were placed on Ni powder and cured at 140 °C for 5 hours. The PEG droplets were very weak, similar to PAA droplets, but the AE droplets were very strong; the 40% solution was not crushable with tweezers. The 20 % AE binder created droplets from pipetting that were strong enough, but when the binder is used in the 3D printer, the saturation will not be as high so the extra strength from 40% AE was thought necessary at lower saturations.

Table 2 Binder Solutions Examined

Solution	Composition	Result
PVA1	2 wt% PVA	No solution tested
PVA2	4 wt% PVA	No solution tested
PEG1	2 wt% PEG	Weak binding
PEG2	4 wt% PEG	Weak binding
AE1	20 vol% AE emulsion	Strong binding
AE2	40 vol% AE emulsion	Very strong binding

The AE2 binder needed to have a viscosity similar to S-type and N-type binders to prevent clogging of the print head. Figure 10 is the rheology data, showing that the viscosity of AE2 was actually lower than S-type binder, making it usable in the 3D printer.

The first 3D printing with AE2 was a 500 μm wire part, printed in 50 μm layers, at 90 % saturation, and 45 second dry time at 90% heater power. When the part was removed after curing 2 hours at 140 °C, it was discovered that the layer strength was very poor; the wires were strong but the connection between layers was weak. This occurred because of rapid drying causing shrinkage before the next layer was printed. To prevent this, subsequent printing had layer dry times of 45 seconds at only 30-40% heater power so that the layer is not fully dry before the next layer is printed. This created parts with high green strength that could be removed from the powder bed.

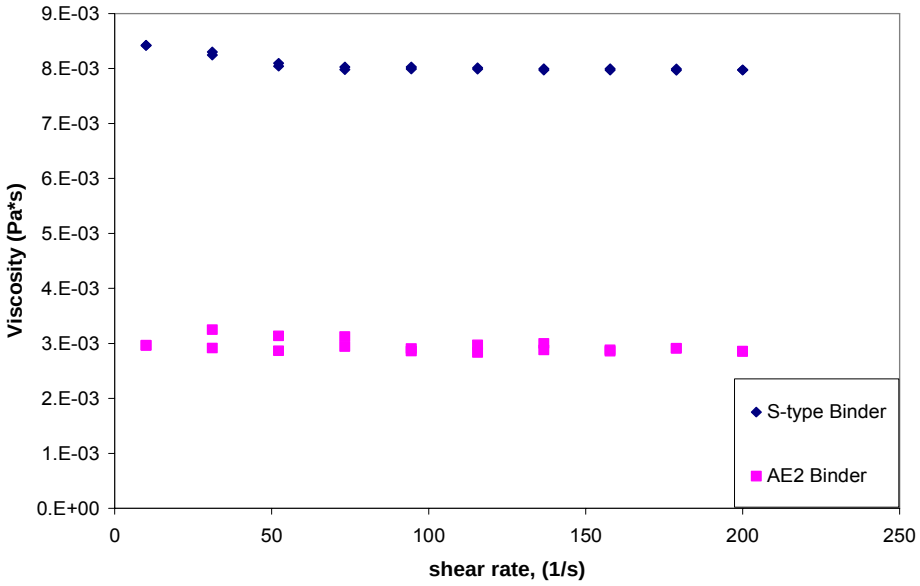

Figure 10 Rheology of S-binder and AE2 Binder

Print head Cleaning

An acrylic emulsion creates additional challenges in cleaning the 3D printer print head. If the emulsion polymerizes then the nozzles of the print head will be easily clogged. Experience has showed that the print head cap needs to be flushed with cleaner after every layer so that the surface of the print head is cleaned on capping. In addition, immediately after the print job is finished the print head needs to be flushed with cleaner to prevent the binder from clogging the print head. Different cleaners have been used in the ultrasonic cleaner to unclog a print head but with little success.

NiTi Powders

A fine NiTi powder (-635 mesh) was acquired from Crucible Research (Pittsburg, PA) to ensure that AE2 binder would work satisfactorily with an alloy composition similar to the final TiNiHf to be used. The NiTi powder was compared with the Ni powder under SEM to qualitatively assess particle shape and size as seen in Figure 11.

The particle size was similar for both powders but the shape of NiTi particles were more spherical with less surface porosity.

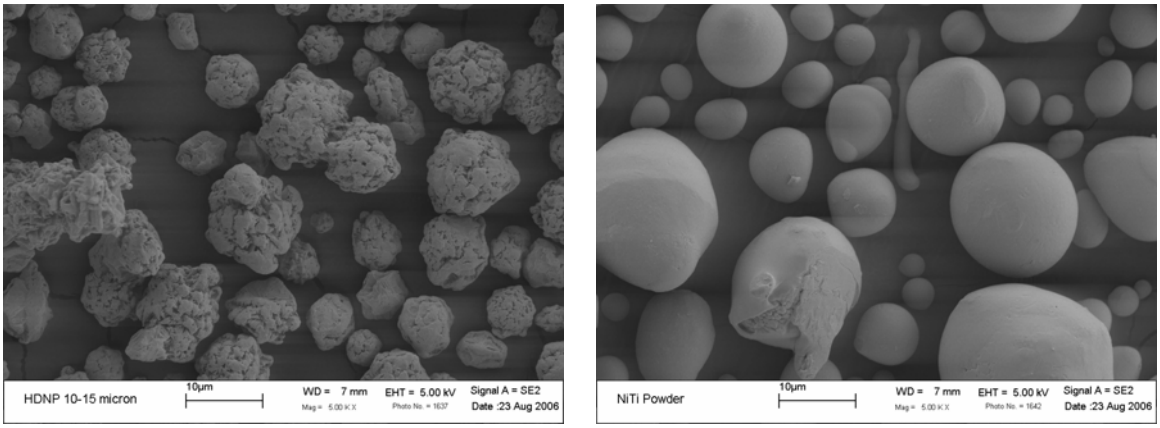

Figure 11 Pure Ni (left) and NiTi (right) powders

When the NiTi powder was 3D printed, it was observed that the powder flowed better than Ni powder. Also, the AE2 binder wet the particles very well and made stronger parts than with Ni powder.

Bi-layer Test Fixture Development

The sealing ability of the SLABS glass and the SLABS / SMA composite samples needs to be tested so a test fixture which allows for control of temperature and internal helium pressure was developed. By controlling internal pressure of sealed samples, SOFC operating conditions can be simulated for the sealant material. Helium is a good substitute for the hydrogen used in SOFC because of it's light weight and ideal gas behavior. The important sealant property to be studied is leak rate, which can be calculated since pressure is being constantly monitored. By measuring pressure drop, the internal volume of the tubing and the ideal gas law can determine the mass of He leaking from the test fixture.

A schematic of the test fixture is shown in Figure 12. ¼" stainless steel tubing connects a helium tank to the internal chamber of the bi-layer test sample through a ball valve, a needle valve, a pressure gauge, and a pressure transducer. The ball valve, needle valve, and pressure gauge are used to set the pressure to a desired value when initializing a test. When tests are conducted, a National Instruments (Austin, TX) data acquisition meter is used to constantly monitor the pressure from an Omega (Stanford, CT) pressure transducer and temperature from a K-type thermocouple.

To make an airtight bond between the ¼" tubing and the E-brite stainless steel sheet, a Cu-Zn flux coated braze was used. The braze has a melting temperature of 850-900ºC which is above the sample testing temperature of 800ºC. A typical braze is shown in Figure 13, and these samples have adequately sealed the E-brite sheet to the tubing and withstood an 800ºC heating to burn off the flux.

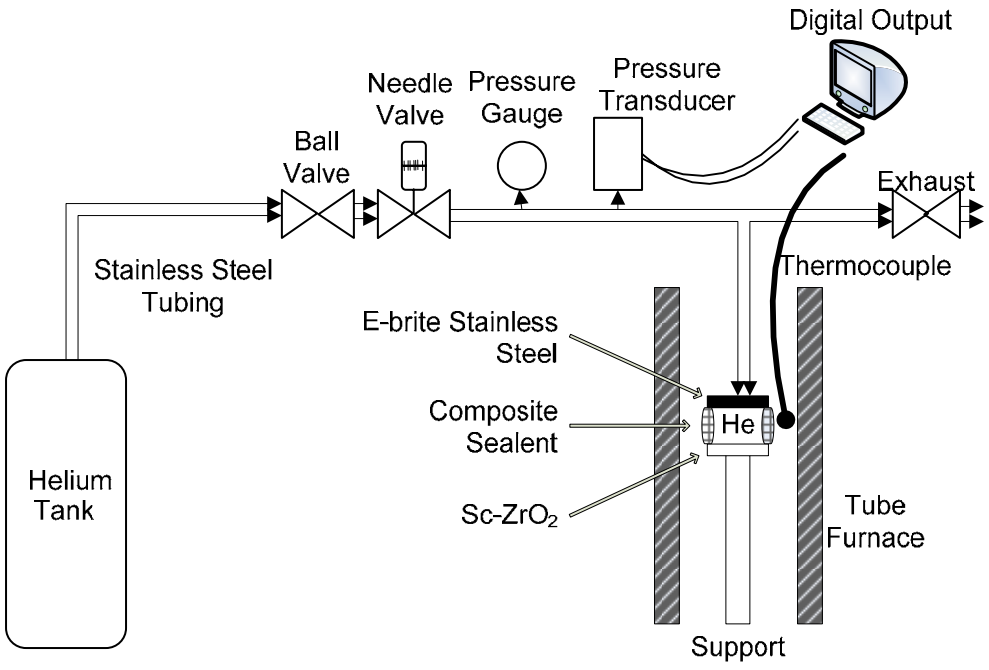

Figure 12 Design of Bi-layer Test Fixture

Figure 13 E-brite stainless steel Cu-Zn brazed to ¼" stainless steel tubing

SMA / SLABS Sintered Powders

To investigate the interaction of the two seal materials, mixed powders of varying compositions were sintered and examined under an optical microscope, scanning electron microscope, and an energy dispersive spectroscopy system.

Sample Preparation

SLABS glass frit was spex milled to <100 mesh (~150 μm) and mixed with either 10 or 40 wt% NiTiHf powder (<635 mesh). An acrylic binder was used and the samples were pressed in a steel mold to ~90 MPa to make samples 2.5×2.5×0.25 cm. After drying, the samples were sintered in vacuum (2.6×10^{-6} torr) by heating at 3ºC/min to 500ºC for a 3 hour binder burn-out and to 1000ºC for a 3 hour sinter. They were subsequently thermally cycled four times in air at 3 ºC/min from 50ºC to 800ºC.

Optical Microscopy of SMA/SLABS Sintered Samples

The 10wt% and 40wt% SMA samples were mounted, polished, and examined under an optical microscope. It is clear that there is porosity in both samples, Figure 14 and Figure 15, but the 10wt% SMA sample has closed pores, while the 40wt% SMA

sample is not fully sintered and has a network of open pores. Interconnected pores could lead to a higher degree of oxidation in the samples and would allow gas leakage through the sealant material.

There is oxidation of the NiTiHf particles in the 10wt% SMA sample as seen in Figure 16. The particle centered in Figure 16 has a diameter of ~12 μm and there is a reaction zone approximately 2-4 μm around the particle. These reaction zones were visible around all particles in the material and were also observable in the 40wt% sample. No microscopy was performed on the samples after vacuum sintering so it is not apparent whether the reaction happened during vacuum sintering at 1000ºC or during cycling in air at 800ºC. Excessive reaction during either of these two thermal profiles is unacceptable.

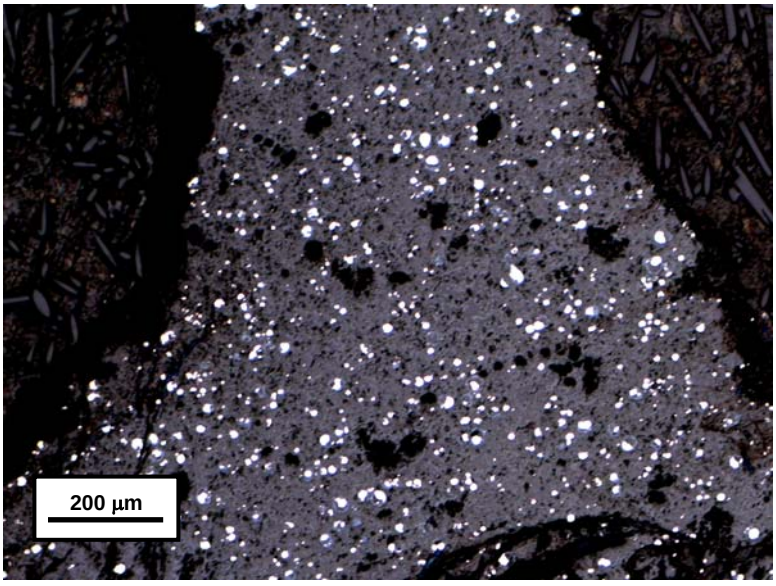

Figure 14 Optical Micrograph of 10wt% NiTiHf Sintered Sample

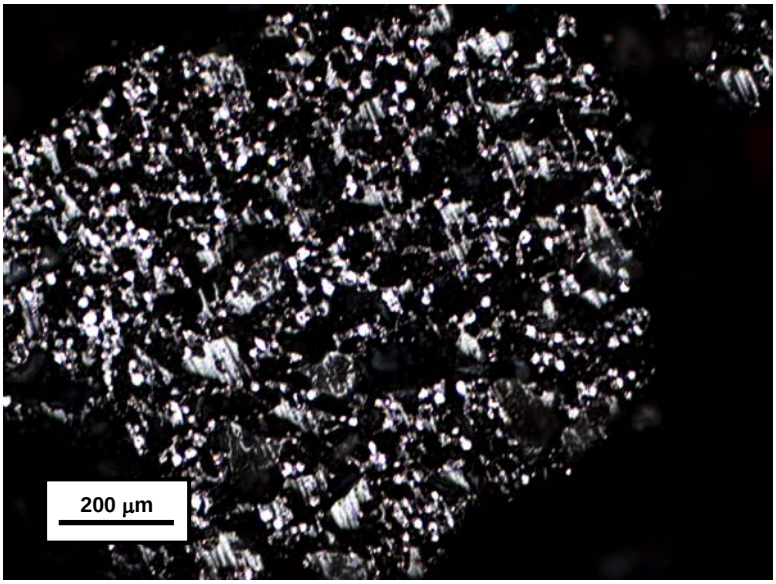

Figure 15 Optical Micrograph of 40wt% NiTiHf Sintered Sample

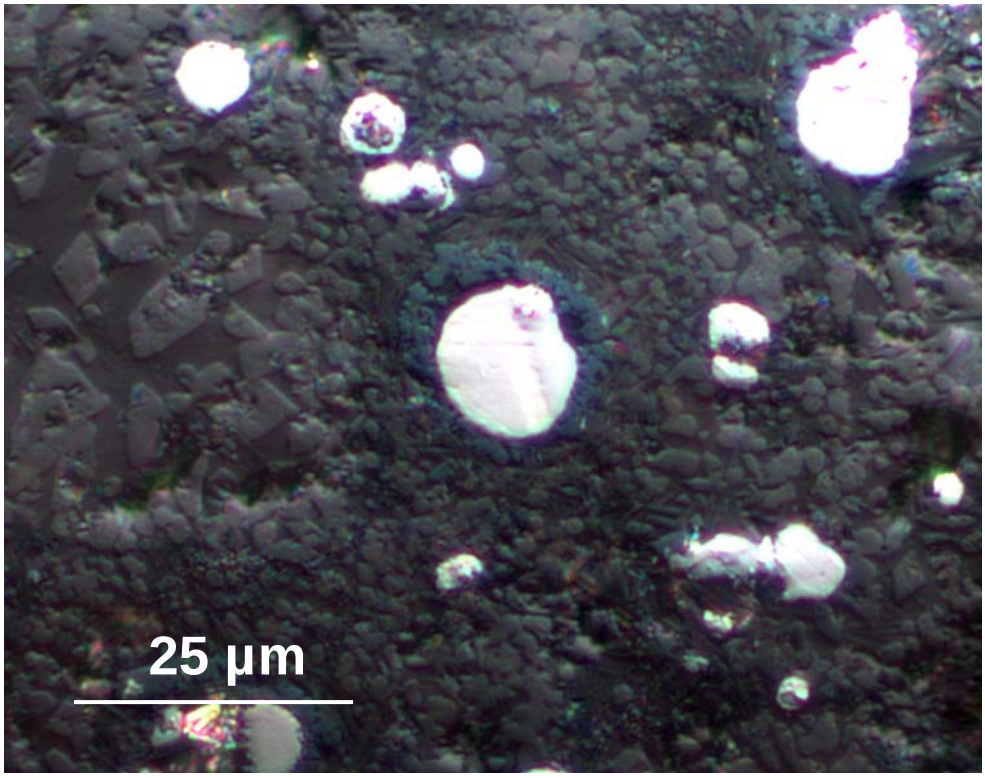

Figure 16 Optical Micrograph of reaction zone around NiTiHf particles in 10wt% NiTiHf sample

Electron Microscopy and EDS

The reaction zone around the particles was further studied with a scanning electron microscope and energy dispersive spectroscopy system. Both the 10wt% and

40wt% samples were examined. The SLABS amorphous phase and crystalline phase, in addition to SMA particles can be seen in Figure 17, but there is another needle-shaped phase seen as well. This phase is also visible in the 40wt% sample under the SEM, but the phase was not seen in either sample under the optical microscope. It is important that the needle-shaped phase, though not directly surrounding, was always in the vicinity of SMA particles.

The EDS line scan detected all of the sealant elements with the exception of boron, but silicon and aluminum are not presented because they only showed noise due to low atomic percents in the composition. Looking at the SLABS elements, Sr and La, it is seen that they are not congruent. They both have minima where the SMA particle is scanned, but at the very right of the scan, they have opposing peaks signifying that the SLABS crystalline and amorphous peaks have different compositions.

At the scanned SMA particle, oxygen also is at a minimum indicating that the SMA particle is still metallic; however, the SMA elements show contrasting behavior. The Hf and Ti have diffused away from the SMA particle and from each other. The SMA particle is almost entirely Ni, while the Hf and Ti are in the region of the needle-like phase. This diffusion, of course, will eliminate the ability for a shape memory effect. During the vacuum sintering or air thermal cycling, the Hf and Ti diffused out of the SMA particles and reacted with the SLABS glass. It is not clear what the reaction product is, and it is important to note, that the EDS system could not detect the high boron content in the glass to determine if the diffusion was due to the high activity of boron. Future work could determine the composition of this reaction product.

Future sintered samples should have either a protective oxidation barrier coating on the SMA particles, or should employ a different lower temperature sintering process to prevent reaction. The neutron diffraction study showed that it is possible to create the SME from NiTiHf alloy embedded in a glass. However, this microscopy and EDS revealed that composition is important to how stable the alloy can be in the glass. If it is not feasible to adequately protect the SMA from the SLABS glass, then it would be necessary to drastically change the glass composition to prevent reaction and diffusion.

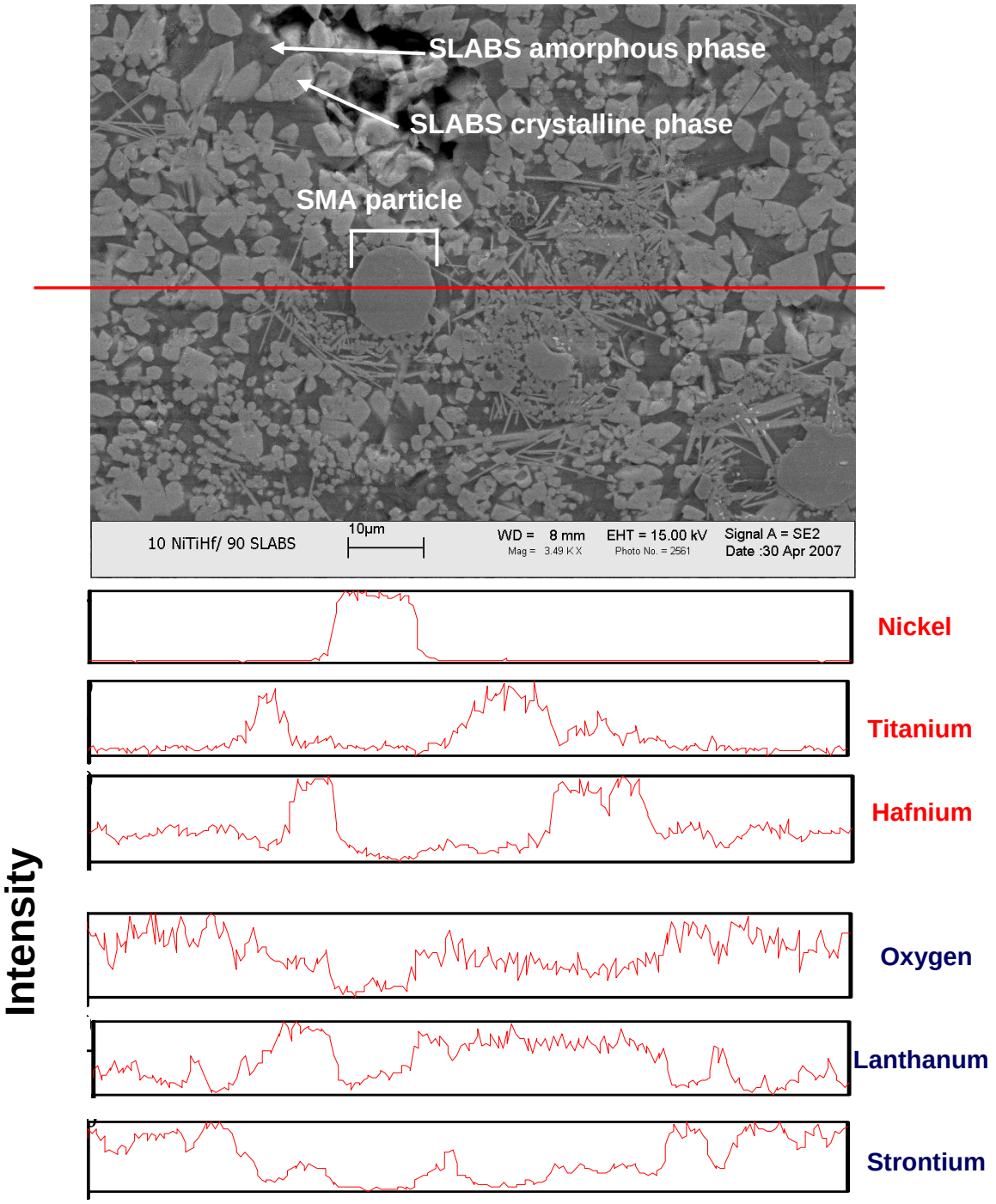

Figure 17 SEM micrograph and EDS line scan of 10wt% SMA sintered composite

Conclusions

A SrO-La_2O_3-Al_2O_3-B_2O_3-SiO_2 glass/ceramic and TiNiHf alloy were produced and characterized by dilatometry, X-ray diffraction, and differential scanning calorimetry. The SLABS glass/ceramic crystallized during thermal cycling to SOFC operating temperatures and that caused an unstable CTE. Differential scanning calorimetry revealed the shape memory phase change occurred between 200 and 250°C. The shape memory effect was also observed in neutron diffraction and distinctions between the bare SMA alloy and SMA/glass composite samples were apparent. The difference between corresponding d-spacings in the SMA/glass composite relative to those in a stress-free SMA indicate residual stresses in the glass is transferred to the SMA of the SMA/glass composite. This shift decreased after the martensite transition, and that suggests twin motion or reorientation in martensite decreases residual stress. In addition, the variations in d-spacings with temperature obtained by neutron diffraction were in good agreement with the CTE of the shape memory alloy measured with dilatometry. Important 3D Printing variables were determined and were modified to create high quality wire meshes from Ni and NiTi powders. A new acrylic binder solution was created which permitted printing of thinner layers from smaller particle size powders. A test fixture for assessing leak rate through sealant materials was designed and constructed. A reaction occurred around the perimeter of the SMA particles and there was diffusion of the SMA species out of the particles.

Future work will focus on suppressing crystallization of the SLABS system to maintain a high CTE. Additionally, the reaction products in sintered SMA/SLABS samples will be determined. Because of the reaction, a reaction barrier coating, lower sintering temperature, or different glass composition will need to be used. Leak testing of

sintered SLABS/SMA composite samples will be conducted to analyze the seal's ability to prevent crack formation and self-heal cracks.

References

[1] Dissemination of IT for the Promotion of Materials Science (DoITPoMS). Univerity of Cambridge. http://www.doitpoms.ac.uk/tlplib/fuel-cells/

[2] K.S. Weil and J.S. Hardy, "Development of a Compliant Seal for Use in Planar Solid Oxide Fuel Cells," 28th International Conference on Advanced Ceramics and Composites, E. Lara-Curzio and M.J. Readey, eds. 25, pp. 321-326, American Ceramic Society, Cocoa Beach, FL, 2004.

[3] R.H. Singh, "High Temperature Seals for Solid Oxide Fuel Cells," 28th International Conference on Advanced Ceramics and Composites, E. Lara-Curzio and M.J. Readey, eds. 25, pp. 299-307, American Ceramic Society, Cocoa Beach, FL, 2004.

[4] R. Loechman, "Development for High Performance Seals for Solid Oxide Fuel Cells," SECA Core Technology Program Review, 2003, Albany, NY.

[5] Y.-S. Chou and J.W. Stevenson, "Long-Term Thermal Cycling of Phlogopite Mica-Based Compressed Seals for Solid Oxide Fuel Cells," Journal of Power Sources, 140, 340-345, 2005.

[6] J.W. Fergus, "Sealants for Solid Oxide Fuel Cells," Journal of Power Sources, 147, 46-57, 2005.

[7] R. Kirsch, Metals in Glassmaking, Elsevier, p. 353 and p. 288. 1993.

[8] K.L. Ley et. al., "Glass-Ceramic Sealants for Solid Oxide Fuel Cells: Part 1. Physical Properties," Journal of Materials Research, 11, 6, 1489-1493.

[9] X.L. Meng et. al., "Two-way Shape Memory Effect of a TiNiHf High Temperature Shape Memory Alloy," *Journal of Alloys and Compounds*, 372, 180-186, 2004.

[10] P.L. Potapov, A.V. Shelyakov, A.A. Gulyaev, E.L. Svistunova, "Effect of Hf on the Structure of Ni-Ti Martensitic Alloys," *Materials Letters*, 32, 247, 1997.

[11] X.L. Wang, Y.D. Wang and J.W. Richardson, "Experimental error caused by sample displacement in time-of-flight neutron diffractometry," *Journal of Applied Crystallography,* 35, 533-537, 2002.

[12] Holman, R. K., et al., *J. of Colloid and Int. Science*, 247, 266-274 (2002).

Vita

Christopher B. Story was born in Orange County, CA on August 29, 1984. He completed his bachelor's degree at Virginia Tech in May 2006 with his senior design project on an internally reinforced bonding technique for titanium alloys to carbon/epoxy composites. In 2004 he was in the study abroad program at the University of Sheffield, England. He has interned twice at NASA Langley Research Center in the Metals and Thermal Structures Branch working on sol-gel coatings for oxidation protection of nickel-based superalloys, and on testing ceramic repair materials and fasteners for holes in the Space Shuttle tiles and carbon/carbon leading edge. His interests are in applied materials engineering for energy and transportation applications. The date of his Masters thesis defense was May 8, 2007.